Anisotropic statistical scaling of soil and sediment texture in a stratified deep vadose zone near Maricopa, Arizona

A. Guadagnini [a,b,*], S.P. Neuman [b,1], M.G. Schaap [c], M. Riva [a,b]

[a] Dipartimento di Ingegneria Civile e Ambientale, Politecnico di Milano, Piazza L. Da Vinci, 32, 20133 Milano, Italy
[b] Department of Hydrology and Water Resources, University of Arizona, Tucson, AZ, USA
[c] Department of Soil, Water and Environmental Science, University of Arizona, Tucson, AZ, USA

Article history:
Received 21 May 2013
Received in revised form 30 August 2013
Accepted 12 September 2013
Available online 7 October 2013

1. Introduction

Soils are ubiquitously structured and heterogeneous, exhibiting spatial and directional variations on a range of scales. Western et al. (2002) consider a triplet of scales expressed in terms of data spacing, support and extent. Neuman and Di Federico (2003) discuss isotropic and directional dependencies on scales of measurement (data support), observation (extent of flow-related phenomena such as a dispersing solute plume), sampling window (domain of investigation), spatial correlation (structural coherence), and spatial resolution (descriptive detail). Direction and/or scale dependent spatial statistics of sedimentary rock and soil hydraulic properties have been analyzed (among others) by Hewitt (1986), Molz and Boman (1993), Molz et al. (1997), Deshpande et al. (1997), Tennekoon et al. (2003), Castle et al. (2004), Guadagnini et al. (2012a), Riva et al. (in press), and Zimmermann et al. (2013).

Spatial (and/or temporal) increments of hydrogeophysical data are often associated with heavy-tailed sample frequency distributions (e.g., Painter, 1996; Yang et al., 2009; Riva et al., 2013, in press). In some cases, these distributions display a transition from heavy tailed to near Gaussian with increasing separation scale or lag (Liu and Molz, 1997; Painter, 2001; Ganti et al., 2009; Riva et al., 2013, in press; Guadagnini et al., 2012a). Liu and Molz (1997), Riva et al. (2013, in press) and Guadagnini et al. (2012a) analyzed spatial increments of log hydraulic conductivities in various laboratory and field settings, finding their frequency distributions to be reasonably well represented by a Lévy- or

* Corresponding author. Tel.: +39 02 2399 6263.
E-mail addresses: alberto.guadagnini@polimi.it (A. Guadagnini), neuman@hwr.arizona.edu (S.P. Neuman).
[1] Tel.: +1 520 621 7114, +1 520 621 5082(Dept. Phone).

α-stable distribution (Samorodnitsky and Taqqu, 1994). These distributions have power-law tails characterized by a positive Lévy or stability index, α, that decreases from 2 in the Gaussian case to 1 (or less in theory) as the tails widen.

Much less has been done and published about direction and scale dependent spatial statistics of soil and sediment texture characteristics (such as percent sand, silt, clay and bulk density) which in turn impact the associated hydraulic properties (e.g. porosity, saturated hydraulic conductivity and constitutive relationships between relative hydraulic conductivity, capillary pressure and saturation); most related publications consider particle-size indicators to scale (contrary to our findings below) as multifractals (Miranda et al., 2006; Zeleke and Si, 2006; Vidal Vázquez et al., 2008; Wang et al., 2008; Martín et al., 2009). In this paper we analyze the statistical scaling properties of soil and sediment texture data measured to a depth of 15 m over an area of 3600 m^2 in a vadose zone near Maricopa, Arizona. The data include soil composition in terms of sand, silt and clay fractions as well as their principal components and logit transforms. The logit transform allows extending the support of variables constrained between upper and lower limits (such as 0 and 1 in the case of sand fraction) to the infinite domain of positive and negative real numbers.

2. Materials and methods

2.1. Site description

Work at the Maricopa site was initially funded by the U.S. Nuclear Regulatory Commission with the aim of improving our ability to monitor and model water flow and solute transport in a deep vadose zone analogous to that found at the (now defunct) Yucca Mountain, Nevada, potential underground high level nuclear waste repository site (Young et al., 1999; Thomasson and Wierenga, 2003; Wang et al., 2003). Additional characterization of soil and sediment texture and hydraulic property distributions, as well as flow modeling, at the Maricopa site were conducted for scientific purposes a few years later under the auspices of the U.S. National Science Foundation (Fang, 2009; Schaap, 2013). The site is located in a broad alluvial valley with thick near-horizontal sedimentary deposits that vary between gravel and clay with a fine loamy soil at the surface. The complex has been sampled at 1029 locations along several vertical boreholes and a horizontal transect, shown in Fig. 1. As bulk density data are limited to the upper 5 m of the soil profile, we focus our analysis in this paper on particle size samples collected down to a depth of 15 m. Additional details about the site and the sampling procedure are given by Schaap (2013).

2.2. α-Stable distributions

We noted in the Introduction that frequency distributions of spatial increments in a range of variables are reasonably well represented by a Lévy- or α-stable distribution (Samorodnitsky and Taqqu, 1994). An α-stable probability distribution is characterized by four real-valued parameters: Lévy or stability index $\alpha \in (0, 2]$, skewness $\beta \in [-1, 1]$, scale $\sigma > 0$ and shift μ. The distribution is defined by its characteristic function written, among other possible forms (Samorodnitsky and Taqqu, 1994), as

$$\ln\left\langle e^{i\phi Z}\right\rangle = i\mu\phi - \sigma^{\alpha}|\phi|^{\alpha}[1 + i\beta\,\mathrm{sign}(\phi)\omega(\phi,\alpha)]; \quad \omega(\phi,\alpha) = \begin{cases} -\tan\frac{\pi\alpha}{2} & \text{if } \alpha \neq 1 \\ \frac{2}{\pi}\ln|\phi| & \text{if } \alpha = 1 \end{cases} \tag{1}$$

where Z is an α-stable variable, $\langle\rangle$ represents expected value (ensemble mean), ϕ is a real-valued parameter and $\mathrm{sign}(\phi) = 1, 0, -1$ if $\phi > 0, = 0, < 0$, respectively. When $\alpha = 2$ the distribution becomes Gaussian. In Section 3 below we compute an estimate $\hat{\boldsymbol{\theta}} = \left(\hat{\alpha}, \hat{\beta}, \hat{\sigma}, \hat{\mu}\right)$ of the parameter vector $\theta = (\alpha, \beta, \sigma, \mu)$ by the maximum likelihood (ML) method using the computer code STABLE developed by Nolan (2001). ML entails maximizing the likelihood

$$l(\boldsymbol{\theta}) = \sum_{j=1}^{n} \log f\left(Z_j|\boldsymbol{\theta}\right) \tag{2}$$

with respect to $\boldsymbol{\theta}$ where z_j is the jth sample of Z n is sample size and $f(Z|\boldsymbol{\theta})$ the conditional probability density function (pdf) of Z. STABLE yields reliable estimates of stable densities for $\alpha > 0.1$. A detailed description of the STABLE algorithm is given by Nolan (1997).

3. Results and discussion

3.1. Statistical analysis of particle size data

Our analysis focuses on particle size data given as fractions f_i, $0 \le f_i \le 1$, of three texture categories $i = sa$, si and cl representing sand, silt and clay, respectively. We employ the US Department of Agriculture (USDA) classification according to which particles having diameters of less than 0.002 mm are categorized as clay, those having diameters between 0.002 mm and 0.05 mm form silt, and all larger particles constitute sand. A textural triangle of all particle-size samples (Schaap, 2013) indicates that most fall into sand, loamy sand and sandy loam textural classes and relatively few into loam, clay loam, sandy clay loam and silt loam classes. The data delineate an elongated

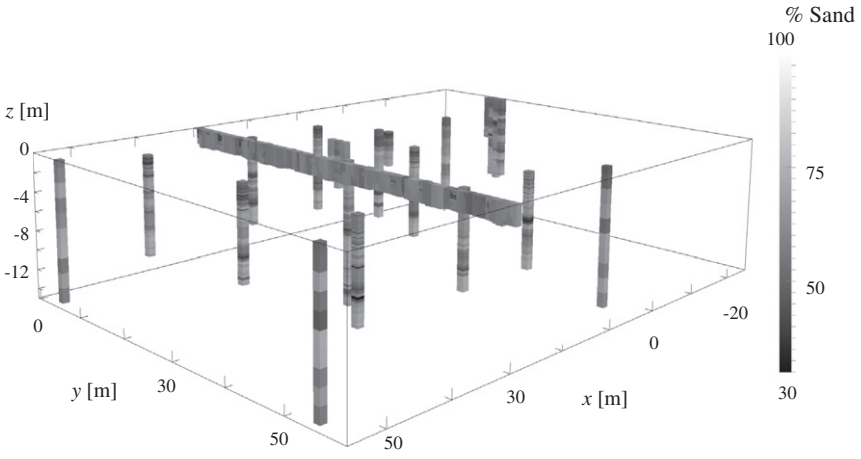

Fig. 1. Spatial distribution of the sampling network at Maricopa experimental site. Gray scale represents measured relative sand fraction, f_{sa}.

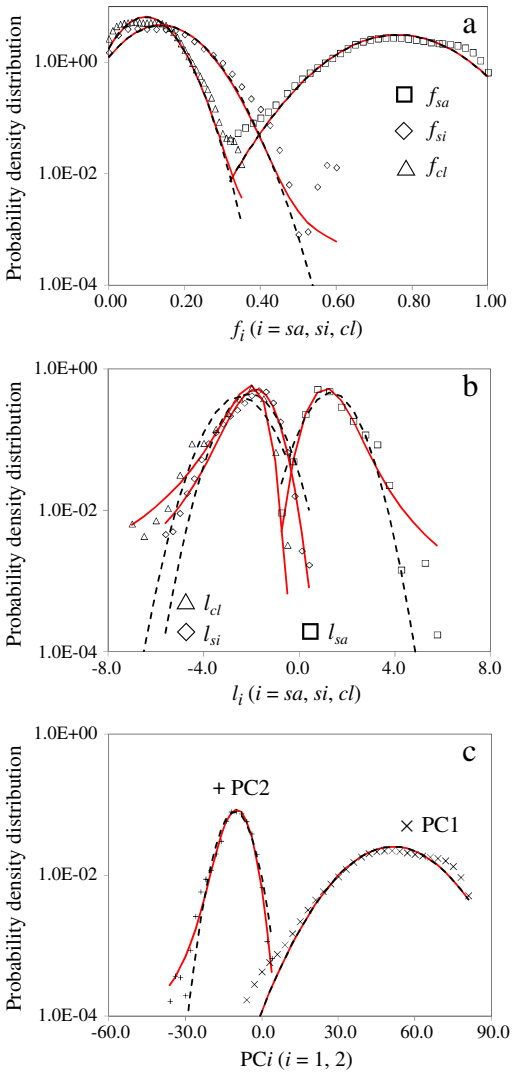

Fig. 2. Frequency distributions (symbols) of (*a*) f_i (i = *sa*, *si*, *cl*), (*b*) $l_i = ln(f_i / (1 - f_i))$ and (*c*) PC1 and PC2 together with α-stable probability density functions (pdfs, solid) fitted to these distributions by ML. Corresponding Gaussian pdfs (dashed) are included for comparison.

cluster of points that suggest a rough correlation between sand and clay fractions caused partly by the need for sand, silt and clay to make up the whole of each sample and partly by the site's depositional history. It is possible to reduce the number of dominant variables from three to two by defining principal components of f_i, labeled PC1 and PC2, parallel and transverse to the longitudinal axis of the cluster. Schaap has done so on the basis of 520 representative samples demonstrating that whereas PC1 carries 92% of the cluster variance due primarily to variations in the sand fraction, PC2 carries 8% of the variance due in large part to fluctuations in the clay fraction. Schaap placed the origin of the coordinates at the triangle center, which renders some of his PC1 and PC2 values negative. We include these, as well as logit transforms $l_i = \ln [f_i / (1 - f_i)]$ of f_i, in our analysis. Logit transforms allow us to extend the support of f_i from the positive unit domain (0,1) to the unbounded domain of all positive and negative real numbers, $(-\infty, \infty)$; we exclude from consideration 11 l_i values corresponding to zero and unit fractions f_i.

Fig. 2 depicts frequency distributions of sampled f_i, l_i, PC1 and PC2 values together with theoretical α-stable pdfs fitted to these distributions according to the methodology described in Section 2.2. Gaussian pdfs, included in Fig. 2 for comparison, are characterized by $\alpha = 2$ and zero skewness. Whereas the tails of a Gaussian pdf decay exponentially, those of stable pdfs with $\alpha < 2$ follow a power law; the smaller is α, the heavier are the tails. Table 1 lists ML parameter estimates of α-stable pdfs depicted in Fig. 2 and their 95% confidence limits. Estimates of the skewness parameter β corresponding to estimates $\hat{\alpha}$ of α close to 2 are not reliable because the pdf is not sensitive to β when $\alpha \to 2$. This is the case with f_{sa}, f_{si}, f_{cl}, PC1 and PC2 in Table 1. We used Kolmogorov–Smirnoff (K–S) and Shapiro–Wilk (W) tests of normality at significance levels of 0.01, 0.05 and 0.10 to evaluate the hypothesis that f_{sa}, f_{si}, f_{cl} and PC1 are Gaussian. Both tests reject the Gaussian hypothesis in all cases except that of f_{sa} which passes the K–S test at significance levels 0.01 and 0.05. Normal probability plots (not shown) support these findings.

Whereas pdfs fitted to f_i and PC1 distributions in Fig. 2 are seen to be near symmetric with mild tails those fitted to l_{sa}, l_{si}, l_{cl} and PC2 are skewed (the first to the right with positive $\hat{\beta}$, the rest to the left with negative $\hat{\beta}$, Table 1) with heavier tails ($1.400 \le \hat{\alpha} \le 1.858$). Principal component PC1, being related largely to the variability of f_{sa}, is characterized by $\hat{\alpha} = 2$ as is the latter; PC2, being related more closely to the variability of f_{si} and f_{cl}, is characterized by $\hat{\alpha} < 2$ as are they.

3.2. Statistical scaling of vertical particle size increments

Next we analyze the statistical distribution and scaling of incremental f_{sa}, f_{si}, f_{cl}, l_{sa}, l_{si}, l_{cl}, PC1 and PC2 values in the vertical direction. We consider vertical separation distances, or lags, s_v, ranging from zero to 8.5 m, slightly more than half the vertical dimension of the sampled soil volume. As noted by Schaap (2013), most wells were sampled at vertical intervals of 0.25 m. This allows us to compute increments at lags 0 m $\le s_v \le$ 1.6 m by grouping the data into bins of vertical length $\Delta b_v = 0.2$ m, at lags 1.6 m $< s_v \le$ 2.0 m into one bin of length $\Delta b_v =$ 0.4 m, and at larger lags 2.0 m $< s_v \le$ 8.5 m into bins $\Delta b_v = 0.5$ m. We thus obtain a maximum number of 1489 increments at $s_v =$ 2.00 m and a minimum number of 507 at $s_v = 8.50$ m; the total number of vertical (and horizontal) increments for various lags is shown in Fig. S1.

Vertical increments are seen to vary randomly and intermittently throughout the domain. The amplitude of these variations is seen to be largest for sand fraction and smallest for clay fraction. Fig. S2 illustrates this by catenating sequences of vertical increments in f_{sa}, f_{si} and f_{cl} at vertical lags $s_v = 0.4$, 2.0 and 5.0 m. Similar qualitative behavior is exhibited by vertical increments in l_{sa}, l_{si} and l_{cl} as well as by PC1 and PC2 (not shown).

Frequency distributions of vertical increments associated with all variables tend to be symmetric and exhibit heavy tails. Fig. 3 depicts,

Table 1
ML parameter estimates of α-stable pdfs fitted to f_{sa}, f_{si}, f_{cl}, l_{sa}, l_{si}, l_{cl}, PC1 and PC2. 95% confidence limits are listed for all estimates but some $\hat{\beta}$, which are unreliable when $\hat{\alpha}$ is close to 2.

Variable	No. of samples	$\hat{\alpha}$	$\hat{\beta}$	$\hat{\sigma}$	$\hat{\mu}$
f_{sa}	1029	2.000	N/A	0.090 ± 0.040	0.763 ± 0.007
f_{si}	1029	1.989 ± 0.029	0.146	0.059 ± 0.003	0.138 ± 0.005
f_{cl}	1029	1.989 ± 0.029	0.326	0.043 ± 0.002	0.098 ± 0.004
l_{sa}	1018	1.700 ± 0.075	1.000 ± 0.000	0.526 ± 0.027	1.402 ± 0.057
l_{si}	1018	1.700 ± 0.075	−1.000 ± 0.000	0.545 ± 0.028	−2.135 ± 0.058
l_{cl}	1018	1.400 ± 0.162	−1.000 ± 0.000	0.475 ± 0.027	−2.760 ± 0.051
PC1	1029	2.000	N/A	11.14 ± 0.481	51.666 ± 0.963
PC2	1029	1.858 ± 0.060	−0.990 ± 0.028	3.291 ± 0.159	−10.65 ± 0.341

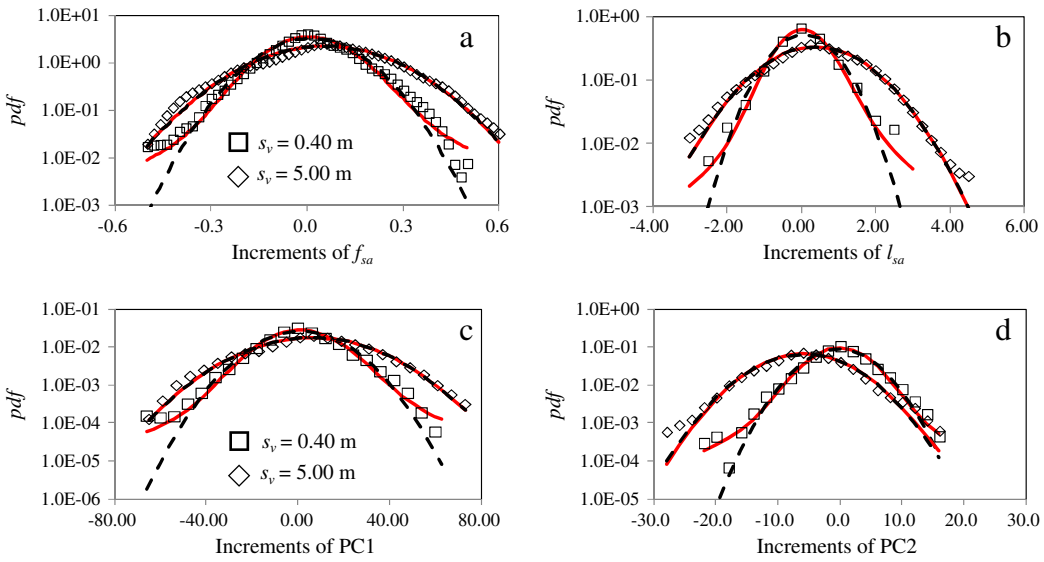

Fig. 3. Frequency distributions of vertical increments of (*a*) f_{sa}, (*b*) l_{sa}, (*c*) PC1, and (*d*) PC2 at two lags. Also shown are ML fits of α-stable (solid) and Gaussian (dashed) pdfs.

as an example, frequency distributions of vertical increments in f_{sa}, l_{sa}, PC1 and PC2 at two lags. Corresponding depictions for all other variables are shown in Figs. S3 and S4. All distributions can be fitted quite closely by ML to α-stable pdfs with parameter estimates $\hat{\alpha}$ and $\hat{\sigma}$ that vary with vertical lag. These variations are illustrated for f_{sa} and l_{sa} in Fig. 4, and for all remaining variables in Figs. S5–S7. Estimates $\hat{\alpha}$ of the stability index α are seen to fluctuate due, we believe, to relative paucity of incremental data near the tails of the distributions. These estimates do nevertheless suggest a tendency of $\hat{\alpha}$ to increase from relatively small values at short lags toward a narrower range of larger values at longer lags: $\hat{\alpha}$ values corresponding to vertical increments of f_{sa} vary between 1.81 and 2.00, those of f_{si} between 1.68 and 2.00, f_{cl} 1.83 and 2.00, l_{sa} 1.65 and 2.00, l_{si} 1.40 and 2.00, l_{cl} 1.69 and 2.00, PC1 1.80 and 2.00 and PC2 1.67 and 1.99. Estimates $\hat{\alpha}$ associated with increments of f_{cl}, l_{cl} and PC2 vary to a lesser extent with lag and tend to be lower than those associated with other incremental variables, implying that distributions of incremental clay fractions tend to exhibit heavier tails across a wider range of lags than do those of other incremental fractions. Kolmogorov–Smirnov and Shapiro–Wilk tests at a significance level of 0.05 do not, in most cases, support a hypothesis that increments associated with estimates $\hat{\alpha} > 1.9$ derive from a Gaussian pdf. We therefore conclude that the frequency distributions of vertical increments in all our variables are consistent with symmetric α-stable pdfs.

Corresponding estimates of the scale or width parameter $\hat{\sigma}$ in Fig. 4 and Figs. S5–S7 show a tendency to increase with lag toward relatively stable asymptotes except in the case of clay: whereas $\hat{\sigma}$ characterizing vertical increments of f_{cl} varies little with lag, that representing increments of l_{cl} never stabilizes.

Next we compute sample structure functions S_N^q defined as qth order statistical moments of absolute increments in a sample of size $N(s)$,

$$S_N^q(s) = \frac{1}{N(s)} \sum_{n=1}^{N(s)} |\Delta y_n(s)|^q \tag{3}$$

where $\Delta y_n(s) = y(x_n + s) - y(x_n)$ is a sampled increment of a random variable Y over a separation distance s between two points, x_n and $(x_n + s)$, on the x axis. The variable Y is said to exhibit power-law scaling if

$$S_N^q(s) \propto s^{\xi(q)} \tag{4}$$

where the power or scaling exponent, $\xi(q)$, depends solely on the order q. When the scaling exponent is linearly proportional to q, $\xi(q) = H\,q$, Y is said to form a self-affine (monofractal) random field (or process) with Hurst exponent H; when $\xi(q)$ is a nonlinear function of q, Y has traditionally been taken to be multifractal or to form fractional Laplace motion (for a recent discussion see Neuman et al., 2013). Fig. 5 plots sample structure functions of orders 1, 2 and 3 associated with vertical increments of f_{sa} and l_{sa} as functions of vertical lag on logarithmic scale. It is useful to note that $S_N{}^1(s)$ is the mean of absolute sample increments and $S_N{}^2(s)$ is twice the sample semivariogram. In each case there is a mid-range of lags within which the data can be fitted by regression to straight lines at high levels of confidence as indicated by coefficients of determination, R^2, close to 1. We do so by varying the lower and upper lag values delimiting this range and selecting that pair of lags

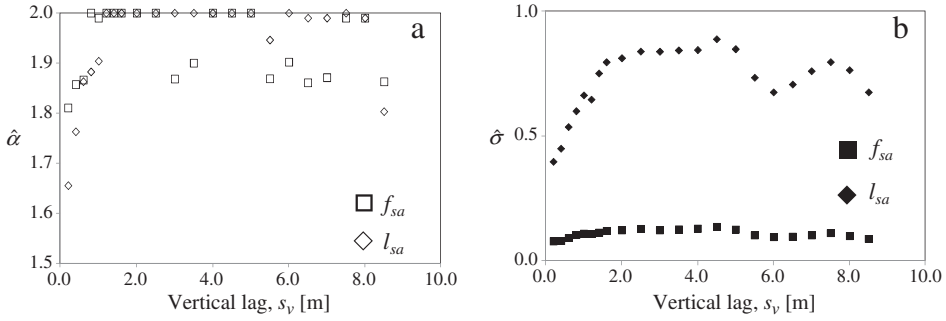

Fig. 4. Variations of ML parameter estimates $\hat{\alpha}$ (*a*) and $\hat{\sigma}$ (*b*) of vertical increments in f_{sa} and l_{sa} with vertical lag, s_v.

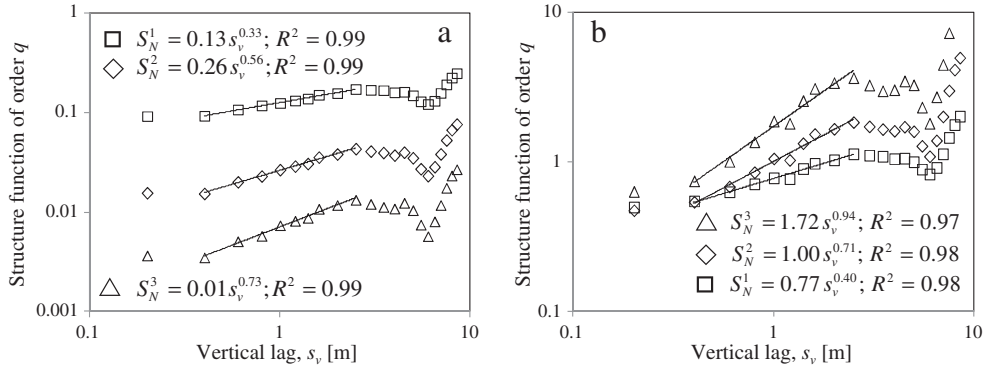

Fig. 5. Sample structure functions of order $q = 1, 2$ and 3 of vertical (*a*) f_{sa} and (*b*) l_{sa} increments versus lag. Regression lines (R^2 values listed) indicate power-law scaling (equations listed) in midranges of lags.

which yields the largest R^2. The fitted straight line implies that, in a midrange of lags, each structure function scales as a power of lag. Fig. 5 lists corresponding power exponents, which we designate by $\xi(q)$, ranging from 0.33 to 0.73 in the case of f_{sa} and from 0.40 to 0.94 in the case of l_{sa}. We refer to this way of determining power scaling exponents for various orders q of a structure function as method of moments (M). Similar scaling behaviors are exhibited by sample structure functions associated with vertical increments of all our variables up to at least order 6.

Another way to determine the manner in which scaling exponents $\xi(q)$ vary with structure function order q is through extended power-law scaling, also known as extended self-similarity or ESS (Siena et al., 2012; Guadagnini et al., 2012b and references therein). We illustrate the approach by plotting in Fig. 6 the dependence of S_N^{q+1} on S_N^q for f_{sa} and l_{sa} at $q = 1$, 2, 3 together with equations of corresponding power law (linear on log–log scale) regression curves and associated coefficient of determination, R^2. Fig. 6 shows that, regardless of q, log S_N^{q+1} varies linearly with log S_N^q (and S_N^{q+1} varies as a power of S_N^q) at all (not just a limited range of) lags. We find the same to be true of all our variables for q values at least as large as 6 (not shown). It follows that, in midranges of lags where S_N^{q+1} and S_N^q scale according to power-law (4), one has log $S_N^{q+1} \propto [\xi(q+1)/\xi(q)]$log S_N^q. This allows us to first evaluate $\xi(1)$ by the method of moments and then to compute $\xi(q)$ for $q = 2, 3, \ldots$ up to any order from successive slopes of ESS curves such as those in Fig. 6 (i.e., from the exponent of the power law fits in Fig. 6).

Fig. 7 compares ways in which power-law scaling exponents $\xi(q)$ obtained for each of our variables by the method of moments, and by ESS at increments $\Delta q = 0.5$, vary with q for $0.5 \le q \le 6.0$. The two methods are seen to yield comparable results. In each case $\xi(q)$ scales in a nonlinear manner with q, delineating a convex curve. Power-law scaling of α-stable increments at intermediate lags, breakdown in power-law scaling at small and large lags, extended power-law scaling to all lags via ESS, and nonlinear variation of the power-law scaling exponent $\xi(q)$ with q have been shown by us elsewhere to be typical of samples from sub-Gaussian random fields or processes subordinated to truncated fractional Brownian motion (tfBm) and/or truncated fractional Gaussian noise (tfGn); for up-to-date descriptions consult Guadagnini et al. (2012b), Siena et al. (2012), Neuman et al. (2013) and Riva et al. (2013, in press).

Whereas nonlinear variation of $\xi(q)$ with q had previously been attributed in the literature to multifractals and/or fractional Laplace motions, we note that fractional Brownian motion (fBm) and/or fractional Gaussian noise (fGn) are monofractal self-affine. Like fBm and fGn, their truncated tfBm and tfGn versions are characterized by a single power-law scaling exponent, H, known as the Hurst coefficient. One way to estimate H is from the slopes of straight lines passing through $\xi(0)$ and $\xi(1)$ in Fig. 7. According to these f_{sa}, f_{si}, f_{cl}, l_{sa}, l_{si}, l_{cl}, PC1 and PC2 are characterized, respectively, by H values estimated with the method of moments equal to 0.33, 0.37, 0.21, 0.40, 0.46, 0.37, 0.34 and 0.21. All of these H estimates are smaller than corresponding estimates of $1/\alpha$, implying that all variables are anti-persistent, varying in a rough rather than a smooth fashion as was the case with f_{sa}, f_{si}, f_{cl} in Fig. S1. Hurst exponents associated with logit transforms are somewhat larger than those associated with particle-size fractions and their principal components. We believe this is due to the transform's stretching of a signal's support, thereby increasing its correlation length and rendering it less rough.

Our finding that vertical increments of particle-size indicators at the Maricopa experimental site exhibit statistical distributions and scaling behaviors typical of samples from sub-Gaussian random fields or processes subordinated to tfBm and/or tfGn allows us to estimate the corresponding Hurst exponents in yet another way. Truncated fBm are autocorrelated

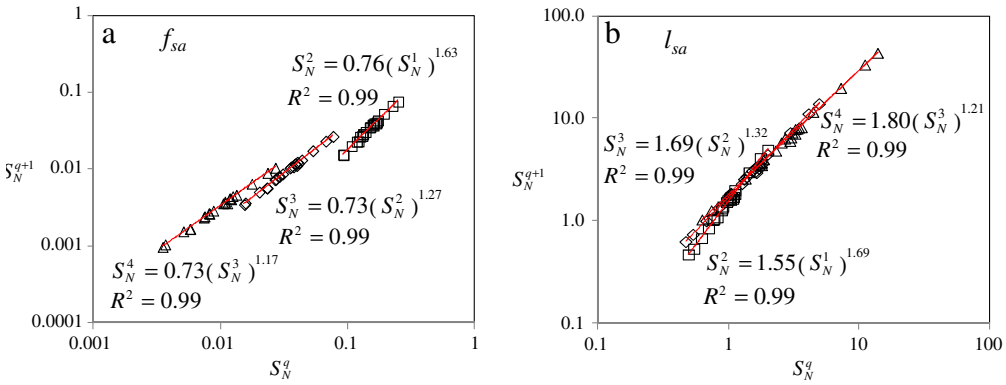

Fig. 6. S_N^{q+1} versus S_N^q for (*a*) f_{sa} and (*b*) l_{sa} at $q = 1, 2, 3$. Regression lines (R^2 values listed) indicate extended power-law scaling (equations listed) at all lags.

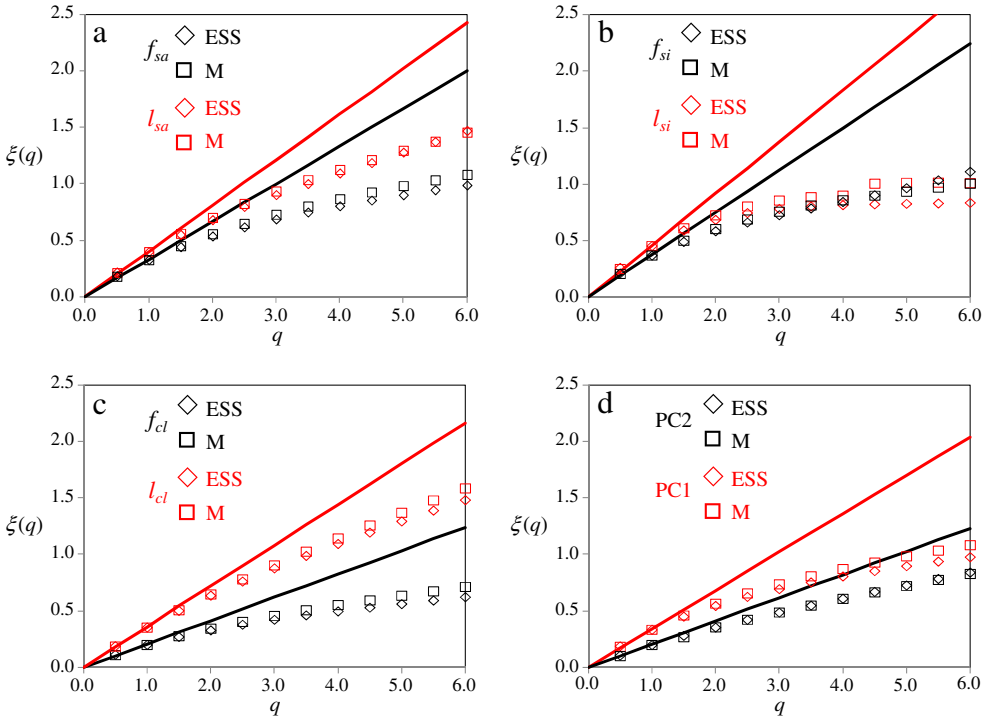

Fig. 7. Variations of power-law scaling exponent $\xi(q)$ with q (symbols) for vertical increments of (*a*) f_{sa} and l_{sa}, (*b*) f_{si} and l_{si}, (*c*) f_{cl} and l_{cl}, and (*d*) PC1 and PC2. Values labeled M were obtained by the method of moments and those labeled ESS by the latter method. Slopes of straight lines passing through $\xi(1)$ and the origin provide estimates of Hurst exponents.

Gaussian random fields or processes, designated here by G, that are characterized by truncated power variograms (TPV or semi structure functions) $\gamma_G^2(s;\lambda_l,\lambda_u)$. The parameters λ_l and λ_u of a TPV represent lower and upper cutoff integral (autocorrelation) scales, respectively, the first proportional to a lower measurement scale or resolution limit on data and the second to an upper domain or window size beyond which data are not sampled. A TPV is fully characterized by its variance and integral autocorrelation scale, which in turn depend on four parameters λ_l, λ_u, H and a coefficient A. Neuman et al. (2008) noted that truncated power variograms arise formally from the sampling of a heterogeneous medium across all geologic categories and scales within an investigation domain. TPV models are able to capture variations of traditional geostatistical parameters, i.e., variogram sill (or variance) and range, which are observed to take place as a function of measurement and sampling domain scales. They are also imbued with the unique ability to represent multiscale random fields associated with either Gaussian or heavy-tailed symmetric probability distributions of the kind we analyze here. Being Gaussian, all moments of G (including structure functions of all orders) are fully defined by its mean and TPV, hence by these same four parameters, which we estimate below. A corresponding subordinated α-stable random field Y, that gives rise to samples such as those represented by our particle-size variables, can be shown theoretically to have scale or width parameter (Samorodnitsky and Taqqu, 1994)

$$\sigma(s;\lambda_l,\lambda_u)=\sqrt{\gamma_G^2(s;\lambda_l,\lambda_u)}; \tag{5}$$

details are given by Eqs. (4)–(13) in Neuman et al. (2013). Having obtained estimates $\hat{\sigma}$ of $\sigma(s;\lambda_l,\lambda_u)$ for each of our variables in Fig. 4 and Figs. S5–S7 thus allows us to estimate the corresponding parameters of $\gamma_G^2(s;\lambda_l,\lambda_u)$.

Table 2
Estimates $\hat{H}$ based on the method of moments and corresponding estimates $\hat{\lambda}_l$, $\hat{\lambda}_u$ and $\hat{I}_v$, as well as $\hat{\sigma}_G^2$ with associated 95% confidence limits (in parentheses) for vertical increments of particle size indicators; estimates $\hat{\lambda}_l \le 10^{-7}$ m are reported as zero.

Variable	$\hat{\lambda}_l$ (m)	$\hat{\lambda}_u$ (m)	$\hat{I}_v$ (m)	$\hat{\sigma}_G^2$
f_{sa}	0.00	1.09	0.44	0.013
($\hat{H}=0.33$ from M)	(–)	(0.42; 1.77)	(0.16; 0.70)	(0.011; 0.015)
l_{sa}	0.03	1.65	0.76	0.62
($\hat{H}=0.40$ from M)	(0.00; 0.24)	(0.86; 2.44)	(0.38; 1.08)	(0.56; 0.68)
f_{si}	0.01	1.37	0.60	0.007
($\hat{H}=0.37$ from M)	(0.00; 0.30)	(0.0; 2.74)	(0.00; 1.16)	(0.006; 0.008)
l_{si}	0.18	1.39	0.77	0.78
($\hat{H}=0.46$ from M)	(0.00; 0.64)	(0.23; 2.56)	(0.11; 1.22)	(0.64; 0.91)
f_{cl}	0.00	0.50	0.15	0.0017
($\hat{H}=0.21$ from M)	(–)	(0.09; 0.91)	(0.02; 0.27)	(0.0015; 0.0018)
l_{cl}	0.00	6.42	2.73	0.69
($\hat{H}=0.37$ from M)	(–)	(1.48; 11.35)	(0.63; 4.82)	(0.49; 0.89)
PC1	0.00	1.12	0.45	206.04
($\hat{H}=0.34$ from M)	(–)	(0.43; 1.80)	(0.17; 0.73)	(179.32; 232.75)
PC2	0.00	1.85	0.55	16.61
($\hat{H}=0.21$ from M)	(–)	(0.48; 3.22)	(0.28; 0.95)	(14.42; 18.80)

As demonstrated theoretically by Siena et al. (2012) the slope of log $\sqrt{\gamma_G^2(s;\lambda_l,\lambda_u)}$ versus log s at intermediate lags, and by implication that of log $\sigma(s;\lambda_l,\lambda_u)$, is equal to the Hurst exponent; one can therefore estimate the latter from corresponding slopes of $\hat{\sigma}$ along their rising limbs in Figs. 4, S5, S6 and S7. This yields estimates $\hat{H}$ equal to 0.21, 0.27, 0.32, 0.39, 0.19, 0.26 and 0.23 for f_{sa}, f_{si}, l_{sa}, l_{si}, l_{cl}, PC1 and PC2, respectively, as compared to 0.33, 0.37, 0.40, 0.46, 0.37, 0.34 and 0.21 obtained for these variables earlier from straight line slopes in Fig. 7. Values of $\hat{\sigma}$ associated with f_{cl} do not show a rising limb and are therefore not amenable to a similar analysis.

Having thus estimated H for each of our variables allows us to estimate all remaining parameters of the corresponding TPVs. We consider TPVs having functional forms given by Eq. (12) in Neuman et al. (2013). We then estimate λ_l, λ_u and A (or, equivalently, σ_G^2) by ML using a public domain code (PEST, Doherty, 2002) which, in our case, is equivalent to minimizing a simple least squares criterion. Results based on H estimates obtained by the method of moments, together with corresponding 95% confidence limits, are listed in Table 2. The table also lists estimates $\hat{I}_v$ of vertical integral scales, I_v, characterizing each TPV according to Eq. (8) in Neuman et al. (2013). Integral scale estimates associated with fractions f_i are generally smaller than those associated with their logit transforms l_i, consistent with our earlier discussion of a similar trend in corresponding H estimates. Whereas integral scale estimates characterizing f_{sa}, l_{sa}, f_{si}, l_{si}, PC1 and PC2 lie within a narrow range between 0.44 and 0.77 m, that of f_{cl} is shorter and of l_{cl} longer.

As noted by Neuman et al. (2008), truncated power variograms are often difficult to distinguish from classical exponential variogram models. This suggests that hierarchical data which have been previously interpreted by traditional variogram models on the basis of some goodness-of-fit criteria, could (and perhaps should) be reinterpreted in light of our findings and the theoretical framework of Guadagnini et al. (2012b), Siena et al. (2012), Neuman et al. (2013) and Riva et al. (2013, in press). In principle, the multiscale cokriging algorithms developed by Neuman et al. (2008) could then be extended to transfer information about the statistics of the underlying Gaussian process across scales. At the same time, the theoretical framework presented by Neuman et al. (2013) can be employed jointly with an analysis of the kind we perform here to generate multiple realizations of sub-Gaussian random fields which are (a) conditional on data, and (b) fully consistent with observed statistical scaling behavior. These could then be employed in the context of stochastic numerical analysis of flow and transport processes in the investigated domain.

We conclude our analysis of vertical increments by comparing in Fig. 8 estimates of scale parameters σ obtained by ML from sample frequency distributions of such increments at various lags and theoretically on the basis of Eq. (5) with estimates of H, λ_l, λ_u and σ_G^2 listed in Table 2. Also depicted in Fig. 8 are 95% confidence limits on the theoretical estimates. Upper and lower confidence limits were computed by setting $\lambda_l = 0$, $\hat{\sigma}_G^2$ to its upper and lower bounds of the corresponding confidence limits and $\hat{\lambda}_u$ to its lower and upper bounds, respectively.

3.3. Statistical scaling of horizontal particle size increments

We complement the above by analyzing the statistical distribution and scaling of incremental f_{sa}, f_{si}, f_{cl}, l_{sa}, l_{si}, l_{cl}, PC1 and PC2 values in the horizontal direction. We do so for horizontal lags, s_h, ranging from zero to $s_h = 52.50$ m. Considering that the relative position of samples at the site entails a horizontal uncertainty of about 1 m (Schaap, 2013), we set the shortest non-zero horizontal lag equal to $s_h = 2.5$ m. Correspondingly the data were grouped into bins of horizontal length $\Delta b_h = 2.50$ m which in turn served to compute increments between pairs of such values within a 5° vertical wedge bounded by horizontal boundaries separated by a vertical distance of 0.5 m. We thus obtained a maximum number of 3494 absolute increments at $s_h = 22.50$ m and a minimum number of 325 such increments at $s_h = 50.00$ m. The numbers of horizontal absolute increments per lag are shown in Fig. S1.

Catenated sequences of horizontal increments (not shown) exhibit random, intermittent fluctuations similar in appearance to those

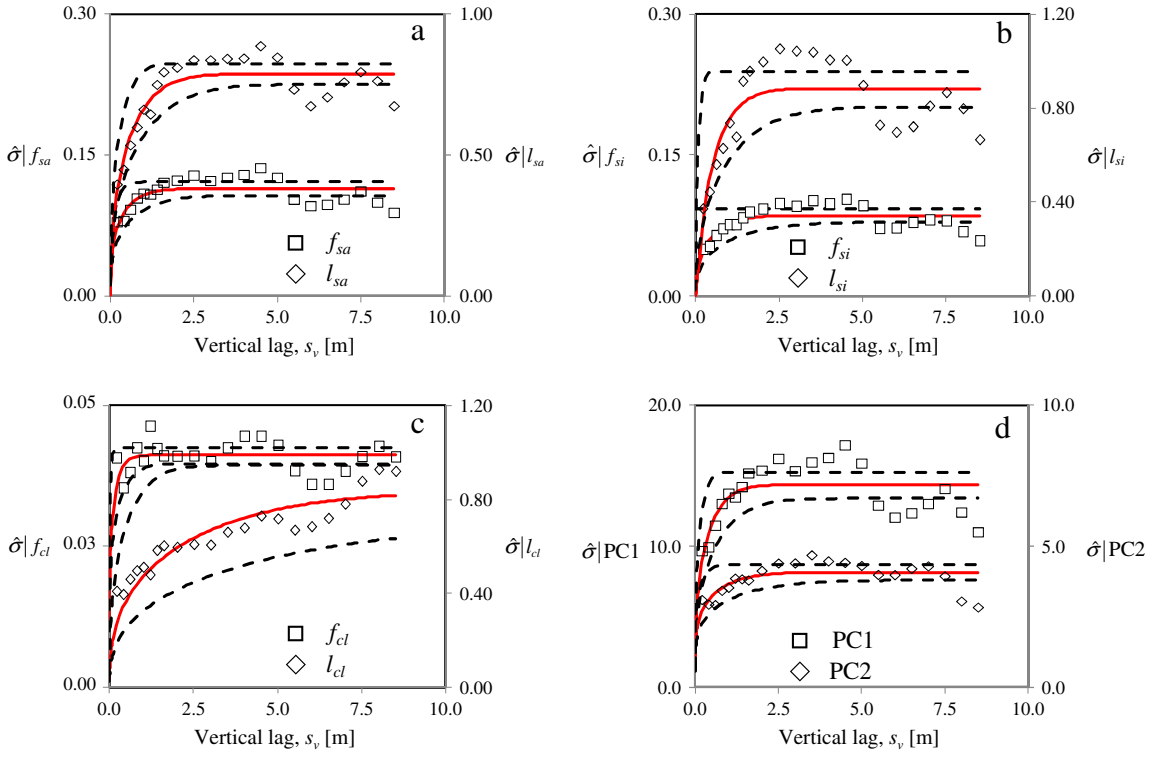

Fig. 8. ML estimates of scale parameters σ (symbols) and their theoretical equivalents (solid curves) based on estimates of H, λ_l, λ_u and σ_G^2 in Table 2 for vertical increments of (*a*) f_{sa} and l_{sa}, (*b*) f_{si} and l_{si}, (*c*) f_{cl} and l_{cl}, and (*d*) PC1 and PC2. Dashed curves represent 95% confidence limits on the theoretical curves.

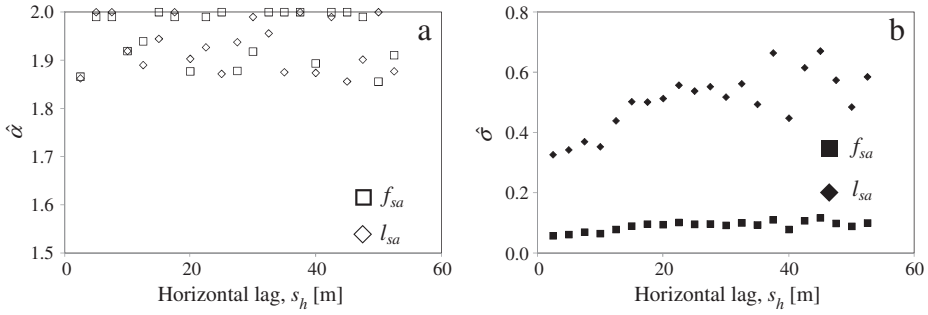

Fig. 9. Variations of ML parameter estimates $\hat{\alpha}$ (a) and $\hat{\sigma}$ (b) of horizontal increments in f_{sa} and l_{sa} with horizontal lag, s_h.

displayed by vertical increments (see Fig. S2). Frequency distributions of horizontal increments, like those of vertical increments in Figs. 3, S3 and S4 tend to be symmetric and exhibit heavy tails (not shown). All distributions can again be fitted by ML to α-stable pdfs with parameter estimates $\hat{\alpha}$ and $\hat{\sigma}$ that vary with lag. Fig. 9 illustrates this behavior for f_{sa}, l_{sa}. Corresponding depictions for all other quantities are found in Figs. S8–S10. As in the case of vertical increments, $\hat{\alpha}$ fluctuates with a tendency to increase from relatively small values at short lags toward a narrower range of larger values at longer lags: $\hat{\alpha}$ values corresponding to horizontal increments of f_{sa} vary between 1.86 and 2.00, those of f_{si} between 1.80 and 2.00, f_{cl} 1.85 and 2.00, l_{sa} 1.86 and 2.00, l_{si} 1.63 and 2.00, l_{cl} 1.65 and 2.00, PC1 1.81 and 2.00 and PC2 1.80 and 2.00. Kolmogorov–Smirnov and Shapiro–Wilk tests at a significance level of 0.05 do, in some cases, support a hypothesis that increments associated with estimates $\hat{\alpha} > 1.9$ derive from a Gaussian pdf (characterized by $\alpha = 2$). We conclude that the frequency distributions of horizontal increments in all our variables are consistent with symmetric α-stable pdfs, some of which tend toward the Gaussian with increasing lag.

Estimates of the scale or width parameter $\hat{\sigma}$ in Figs. 9 and S8–S10 show either a pronounced or a subtle tendency to increase with lag toward relatively stable asymptotes in all cases. This too is consistent with a view of horizontal increments as samples from populations having symmetric α-stable (including Gaussian when α approaches 2) pdfs.

Sample structure functions of absolute horizontal increments exhibit power-law scaling at intermediate lags with breakdown in such scaling at small and large lags (not shown). Estimates $\hat{H}$ of Hurst exponents obtained by the method of moments are very close to those derived from slopes of $\hat{\sigma}$ versus lag (Table 3). All estimates are smaller than $1/\hat{\alpha}$, indicating antipersistence, similar to that observed in Section 3.2 for vertical increments. Estimates $\hat{H}$ for f_{sa} and f_{si}, respectively, are slightly larger and smaller in the horizontal than in the vertical direction. We note however that the unusually small estimates of H obtained by the two methods for PC2 is associated with a relatively small coefficient of determination, $R^2 = 0.66$, rendering them less reliable than other values in Table 3.

Fig. 10 compares ways in which power-law scaling exponents $\xi(q)$, obtained for each of our variables by the method of moments and by ESS, vary with q up to order 6. Results obtained by the two methods differ from each other a bit more than they did in the case of vertical increments (Fig. 7). Though $\xi(q)$ generally scales in a nonlinear manner with q, some of the curves it delineates are convex (as in Fig. 7) while others are concave. Such nonlinear scaling was found by us elsewhere (Guadagnini et al., 2012b; Neuman et al., 2013; Riva et al., 2013, in press) to be typical of samples from sub-Gaussian random fields or processes subordinated to tfBm and/or tfGn.

Table 3
Estimates $\hat{H}$ obtained for horizontal increments by the method of moments (M) and from slopes of $\hat{\sigma}$ (s_h).

Variable	$\hat{H}$ from M	$\hat{H}$ from $\hat{\sigma}$ (s_h)
f_{sa}	0.35	0.35
l_{sa}	0.34	0.35
f_{si}	0.27	0.29
l_{si}	0.24	0.21
f_{cl}	0.24	0.24
l_{cl}	0.27	0.25
PC1	0.35	0.34
PC2	0.09	0.12

Table 4 lists estimates $\hat{\lambda}_u$, horizontal integral scale $\hat{I}_h$ and $\hat{\sigma}_G^2$ for all particle size indicators obtained by ML upon setting $\hat{\lambda}_l = 0$ (following the criteria outlined in Section 3.2) and $\hat{H}$ based on the method of moments. Associated 95% confidence limits are also given. The estimates were obtained by following the same approach as that we had used in Section 3.2 in the context of vertical increments. Integral scale estimates associated with fractions f_i are again smaller than those associated with their logit transforms l_i, though no such trend is now reflected in corresponding H estimates. Horizontal integral scales are larger by one or two orders of magnitude than are vertical integral scales listed in Table 2. This is consistent with soil stratification observed at the Maricopa site by Wang et al. (2003) and Schaap (2013).

Finally we compare in Fig. 11 estimates of scale parameters σ obtained by ML from sample frequency distributions of such increments at various lags and theoretically on the basis of Eq. (5) with estimates of H, λ_l, λ_u and σ_G^2 listed for horizontal increments in Table 4. The figure includes 95% confidence limits on the theoretical estimates. Upper and lower confidence limits were computed in the same manner as in the case of vertical increments (Fig. 8).

4. Summary and specific findings

We analyzed the statistical scaling properties of vertical and horizontal increments in soil and sediment texture variables sampled across a relatively large vadose zone volume near Maricopa, Arizona. Variables included sand, silt and clay fractions f_{sa}, f_{si} and f_{cl}, their principal components PC1 and PC2, and logit transforms l_{sa}, l_{si} and l_{cl}. PC1 and PC2, defined and computed for these samples earlier by Schaap (2013) are dominated by variabilities in sand and in silt and clay fractions, respectively. Logit transforms extend the support of variables constrained between finite upper and lower limits, such as 0 and 1, to the infinite domain of positive and negative real numbers. We found all variables to exhibit statistical scaling properties that are difficult to detect with standard geostatistical methods. These properties include (a) pronounced intermittency (rough, irregular spatial variability) and antipersistence (tendency for large and small values to alternate rapidly); (b) symmetric, non-Gaussian frequency distributions characterized by heavy tails that often decay with separation distance or lag; (c) nonlinear power-law scaling of sample structure functions (statistical moments of absolute increments) in a midrange of lags, with breakdown in such scaling at small and large lags; (d) extended power-law scaling (linear relations between log structure functions of successive orders) at all lags; (e) nonlinear scaling of power-law exponent with order of sample structure function; and (f) pronounced anisotropy in these behaviors. Similar statistical scaling

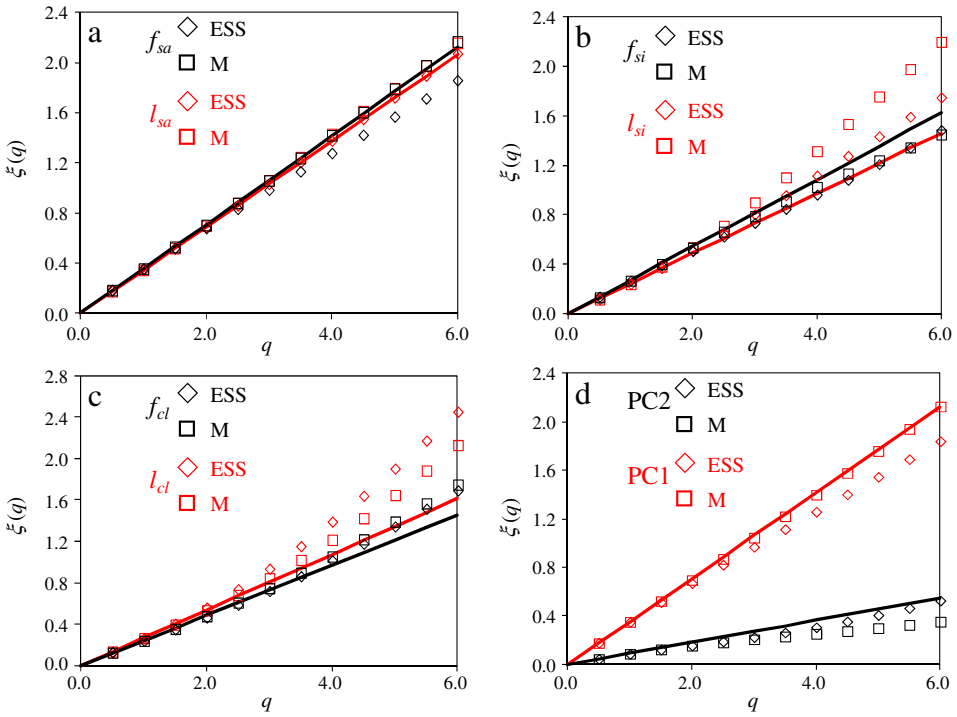

Fig. 10. Variations of power-law scaling exponent $\xi(q)$ with q (symbols) for horizontal increments of (*a*) f_{sa} and l_{sa}, (*b*) f_{si} and l_{si}, (*c*) f_{cl} and l_{cl}, and (*d*) PC1 and PC2. Values labeled M were obtained by the method of moments and those labeled ESS by the latter method. Slopes of straight lines passing through $\xi(1)$ and the origin provide estimates of Hurst exponents.

behaviors are known to be exhibited by a wide variety of earth, environmental and other variables (including ecological, biological, physical, astrophysical and financial). The literature has traditionally interpreted this to imply that the variables are multifractal, which however explains neither the observed breakdown in power-law scaling at small and large lags nor extended power-law scaling. We proposed an alternative interpretation that is simpler and consistent with all the above phenomena. Our interpretation, and corresponding novel method of geostatistical inference, view the data as samples from stationary, anisotropic sub-Gaussian random fields subordinated to truncated fractional Brownian motion (tfBm) or truncated fractional Gaussian noise (tfGn). Such sub-Gaussian fields are mixtures of Gaussian fields with random variances. Truncation of monofractal fBm (which is non-stationary) and fGn entails filtering out components below the measurement or resolution scale of the data and above the scale of their sampling domain. Our new approach allowed us to obtain maximum likelihood estimates of all parameters characterizing the underlying truncated sub-Gaussian fields. These parameters make it possible to downscale or upscale all statistical moments to situations entailing smaller or larger measurement or resolution and sampling scales, respectively. They also allow one to perform conditional or unconditional Monte Carlo simulations of random field realizations corresponding to these scales.

Following is a list of additional, more specific findings:

1. The frequency distribution of each sampled variable at the site can be fitted by the maximum likelihood method (ML) to an α-stable probability density function (pdf). ML-estimated pdfs of most variables are skewed with heavy tails.
2. Vertical and horizontal increments in variables representing sand fraction show larger amplitudes of spatial variations than do those associated with clay fraction, reflecting a relatively small range of values spanned by the latter.

Table 4
Estimates $\hat{H}$ based on the method of moments and corresponding estimates $\hat{\lambda}_u$, $\hat{l}_h$ and $\hat{\sigma}_G^2$ with associated 95% confidence limits (in parentheses) obtained for horizontal increments of particle size indicators upon setting $\hat{\lambda}_l = 0$.

Variable	$\hat{\lambda}_u$ (m)	$\hat{l}_h$ (m)	$\hat{\sigma}_G^2$
f_{sa}	24.59	10.20	0.010
($\hat{H} = 0.35$ from M)	(13.48; 35.71)	(5.59; 14.80)	(0.009; 0.012)
l_{sa}	30.86	12.57	0.337
($\hat{H} = 0.34$ from M)	(13.42; 48.31)	(5.47; 19.68)	(0.272; 0.401)
f_{si}	43.95	15.43	0.006
($\hat{H} = 0.27$ from M)	(14.16; 73.74)	(4.97; 25.89)	(0.004; 0.007)
l_{si}	92.89	30.38	0.618
($\hat{H} = 0.24$ from M)	(0; 259.29)	(0; 84.80)	(0.155; 1.080)
f_{cl}	14.60	4.76	0.0019
($\hat{H} = 0.24$ from M)	(8.27; 20.93)	(2.70; 6.83)	(0.0018; 0.0021)
l_{cl}	19.75	6.90	0.215
($\hat{H} = 0.27$ from M)	(8.37; 31.11)	(2.92; 10.87)	(0.189; 0.241)
PC1	25.65	10.62	161.48
($\hat{H} = 0.35$ from M)	(13.98; 37.31)	(5.79; 15.45)	(138.76; 184.22)
PC2	53.61	8.26	16.23
($\hat{H} = 0.091$ from M)	(0; 137.22)	(0; 21.15)	(12.61; 19.91)

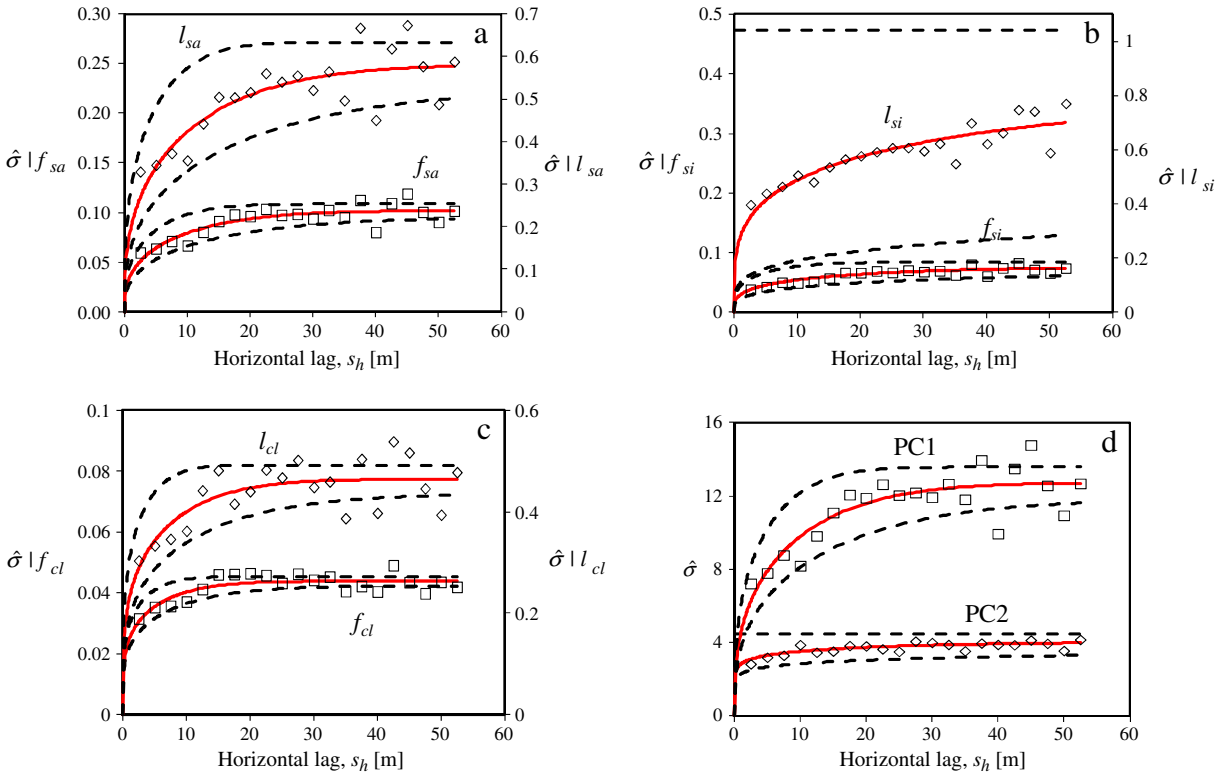

Fig. 11. ML estimates of scale parameters σ (symbols) and their theoretical equivalents (solid curves) based on estimates of H, λ_l, λ_u and σ_G^2 in Table 4 for horizontal increments of (*a*) f_{sa} and l_{sa}, (*b*) f_{si} and l_{si}, (*c*) f_{cl} and l_{cl}, and (*d*) PC1 and PC2. Dashed curves represent 95% confidence limits on the theoretical curves.

3. Frequency distributions of both vertical and horizontal increments, associated with any variable, tend to be symmetric and exhibit heavy tails. All distributions can be fitted quite closely by ML to α-stable pdfs with parameter estimates depending on lag. Tails of the distribution are generally heavier at small than at larger lags. Distributions of vertical and horizontal clay fraction increments tend to show heavier tails across a wider range of lags than do those of other incremental fractions.
4. Power-law exponents of absolute vertical increments in each variable, plotted versus the order of corresponding structure functions, delineate convex curves. Power-law exponents of absolute horizontal increments, plotted in a similar manner delineate convex, concave or near-linear curves.
5. The observed statistical scaling behaviors of vertical and horizontal increments in any variable are consistent with those of samples from sub-Gaussian random fields or processes subordinated to truncated fractional Brownian motion (tfBm) and/or truncated fractional Gaussian noise (tfGn). As such they are fully defined by truncated power variograms (TPVs or semi structure functions of second order) that depend on four parameters: a Hurst scaling exponent H, a lower cutoff scale λ_l proportional to measurement or resolution length scale of the data, an upper cutoff scale λ_u proportional to length scale of the sampling domain or window, and a coefficient A. These parameters in turn define the variance (sill) and integral (autocorrelation) scale of the TPV.
6. The available data allowed us to estimate all parameters of TPVs associated with vertical and horizontal increments of each variable. Our estimates of the Hurst exponent H are consistently lower than those of the inverse stability index, α^{-1}, implying rough antipersistent variability in both the vertical and the horizontal directions of the kind actually demonstrated by the data. Estimates of H associated with vertical and horizontal increments are generally quite similar. On the other hand, estimates of vertical integral scale are smaller by one to two orders of magnitude than those of horizontal integral scale, reflecting the stratified nature of soils at the site. This suggests an elliptical model of statistical scaling anisotropy for tfBm at the site of the kind proposed by Di Federico et al. (1999). The latter in turn allows one to bridge geostatistical information and analysis across scales of data measurement or resolution and sampling domain in a manner similar in principle to that of Neuman et al. (2008).

List of abbreviations

ESS	extended self similarity
fBm	fractional Brownian motion
fGn	fractional Gaussian motion
M	method of moments
ML	maximum likelihood
pdf	probability density function
tfBm	truncated fractional Brownian motion
tfGn	truncated fractional Gaussian motion
TPV	truncated power variogram

Acknowledgements

Our work was supported in part through a contract between the University of Arizona and Vanderbilt University under the Consortium for Risk Evaluation with Stakeholder Participation (CRESP), funded by the U.S. Department of Energy. Funding from MIUR (Italian Ministry of Education, Universities and Research — PRIN2010-11; project: "Innovative methods for water resources under hydro-climatic uncertainty scenarios") is acknowledged.

Appendix A. Supplementary data

Supplementary data to this article can be found online

References

Castle, J.W., Molz, F.J., Lu, S., Dinwiddie, C.L., 2004. Sedimentology and fractal-based analysis of permeability data, John Henry member, Straight Cliffs formation (upper Creta-ceous), Utah, U.S.A. J. Sediment. Res. 74 (2), 270–284.

Deshpande, A., Flemings, P.B., Huang, J., 1997. Quantifying lateral heterogeneities in fluvio-deltaic sediments using three-dimensional reflection seismic data: offshore Gulf of Mexico. J. Geophys. Res. 102 (B7), 15,385–15,402.

Di Federico, V., Neuman, S.P., Tartakovsky, D.M., 1999. Anisotropy, lacunarity, upscaled conductivity and its covariance in multiscale fields with truncated power variograms. Water Resour. Res. 35 (10), 2891–2908.

Doherty, J., 2002. PEST: Model Independent Parameter Estimation, User Manual, 4th ed. Watermark Numerical Computing, Corinda, Queensland, Australia.

Fang, Z., 2009. Using Geostatistics, Pedotransfer Functions to Generate 3D Soil and Hydraulic Property Distributions for Deep Vadose Zone Flow Simulations. The University of Arizona, Tucson (MS thesis).

Ganti, V., Singh, A., Passalacqua, P., Foufoula-Georgiu, E., 2009. Subordinated Brownian motion model for sediment transport. Phys. Rev. E 80 (011111) (doi: 1539-5663755/2009/80(1)/011111(9)).

Guadagnini, A., Riva, M., Neuman, S.P., 2012a. Extended power-law scaling of heavy-tailed random air permeability fields in fractured and sedimentary rocks. Hydrol. Earth Syst. Sci. 16, 3249–3260.

Guadagnini, A., Neuman, S.P., Riva, M., 2012b. Numerical investigation of apparent multifractality of samples from processes subordinated to truncated fBm. Hydrol. Process. 26, 2894–2908. http://dx.doi.org/10.1002/hyp.8358.

Hewitt, T.A., 1986. Fractal Distribution of Reservoir Heterogeneity and their Influence on Fluid Transport, Paper Presented at SPE 61st Annual Technical Conference and Exhibition. Soc. of Pet. Eng, New Orleans, Louisiana, USA.

Liu, H.H., Molz, F.J., 1997. Comment on "Evidence for non-Gaussian scaling behavior in heterogeneous sedimentary formations" by S. Painter. Water Resour. Res. 33, 907–908. http://dx.doi.org/10.1029/96WR03788.

Martín, M.A., Garcia-Gutiérrez, C., Reyes, M., 2009. Modeling multifractal features of soil particle size distributions with Kolmogorov fragmentation algorithms. Vadose Zone J. 8 (1), 202–208. http://dx.doi.org/10.2136/vzj2008.0038.

Miranda, J.G.V., Montero, E., Alves, M.C. Paz, Gonzáles, A., Vidal, Vázquez E., 2006. Multifractal characterization of saprolite particle-size distributions after topsoil removal. Geoderma 134, 373–385. http://dx.doi.org/10.1016/j.geoderma.2006.03.014.

Molz, F., Boman, G., 1993. A fractal-based stochastic interpolation scheme in subsurface hydrology. Water Resour. Res. 29 (11), 3769–3774.

Molz, F., Liu, H., Szulga, J., 1997. Fractional Brownian motion and fractional Gaussian noise in subsurface hydrology: a review, presentation of fundamental properties, and extensions. Water Resour. Res. 33 (10), 2273–2286.

Neuman, S.P., Di Federico, V., 2003. Multifaceted nature of hydrogeologic scaling and its interpretation. Rev. Geophys. 41, 1014. http://dx.doi.org/10.1029/2003RG000130.

Neuman, S.P., Riva, M., Guadagnini, A., 2008. On the geostatistical characterization of hierarchical media. Water Resour. Res. 44, W02403. http://dx.doi.org/10.1029/2007WR006228.

Neuman, S.P., Guadagnini, A., Riva, M., Siena, M., 2013. Recent advances in statistical and scaling analysis of earth and environmental variables. In: Mishra, P.K., Kuhlman, K.L. (Eds.), Advances in Hydrogeology. Springer, New York, pp. 1–15.

Nolan, J.P., 1997. Numerical calculation of stable densities and distribution functions. Commun. Stat. Stoch. Model. 13, 759–774. http://dx.doi.org/10.1080/15326349708807450.

Nolan, J.P., 2001. Maximum likelihood estimation of stable parameters. In: Barndorff-Nielsen, O.E., Mikosch, T., Resnick, S.I. (Eds.), Levy Processes: Theory and Applications. Birkhäuser, Boston, pp. 379–400.

Painter, S., 1996. Evidence for non-Gaussian scaling behavior in heterogeneous sedimentary formations. Water Resour. Res. 32, 1183–1195. http://dx.doi.org/10.1029/96WR00286.

Painter, S., 2001. Flexible scaling model for use in random field simulation of hydraulic conductivity. Water Resour. Res. 37, 1155–1163.

Riva, M., Neuman, S.P., Guadagnini, A., 2013. Sub-Gaussian model of processes with heavy tailed distributions applied to permeabilities of fractured tuff. Stoch. Environ. Res. Risk Assess. 27, 195–207. http://dx.doi.org/10.1007/s00477-012-0576-y.

Riva, M., Neuman, S.P., Guadagnini, A., Siena, M., 2013. Anisotropic scaling of Berea sandstone log air permeability statistics. Vadose Zone J. 12 (3). http://dx.doi.org/10.2136/vzj2012.0153 (in press).

Samorodnitsky, G., Taqqu, M.S., 1994. Stable Non-Gaussian Random Processes. Chapman & Hall, New York.

Schaap, M.G., 2013. Description, analysis and interpretation of an infiltration experiment in a semi-arid deep vadose zone. In: Mishra, P.K., Kuhlman, K.L. (Eds.), Advances in Hydrogeology. Springer, New York, pp. 159–183.

Siena, M., Guadagnini, A., Riva, M., Neuman, S.P., 2012. Extended power-law scaling of air permeabilities measured on a block of tuff. Hydrol. Earth Syst. Sci. 16, 29–42. http://dx.doi.org/10.5194/hess-16-29-2012.

Tennekoon, L., Boufadel, M.C., Lavallée, D., Weaver, J., 2003. Multifractal anisotropic scaling of the hydraulic conductivity. Water Resour. Res. 39, 1193. http://dx.doi.org/10.1029/2002WR001645.

Thomasson, M.J., Wierenga, P.J., 2003. Spatial variability of the effective retardation factor in an unsaturated field soil. J. Hydrol. 272 (1–4), 213–225.

Vidal Vázquez, E., Paz Ferreiro, J., Miranda, J.G.V., Paz González, A., 2008. Multifractal analysis of pore size distributions as affected by simulated rainfall. Vadose Zone J. 7 (2), 500–511. http://dx.doi.org/10.2136/vzj2007.0011.

Wang, W., Neuman, S.P., Yao, T.-M., Wierenga, P.J., 2003. Simulation of large-scale field infiltration experiments using a hierarchy of models based on public, generic and site data. Vadose Zone J. 2 (3), 297–312.

Wang, D., Fu, B., Zhao, W., Hu, H., Wang, Y., 2008. Multifractal characteristics of soil particle size distribution under different land-use types on the Loess Plateau, China. Catena 72, 29–36. http://dx.doi.org/10.1016/j.catena.2007.03.019.

Western, A.W., Grayson, R.B., Bloschl, G., 2002. Scaling of soil moisture: a hydrologic perspective. Ann. Rev. Earth Planet. Sci. 30, 149–180.

Yang, C.-Y., Hsu, K.-C., Chen, K.-C., 2009. The use of the Levy-stable distribution for geophysical data analysis. Hydrogeol. J. 17, 1265–1273. http://dx.doi.org/10.1007/s10040-008-0411-1.

Young, M.H., Wierenga, P.J., Warrick, A.W., Hofmann, L.L. Musil, Hofmann, L.L., Musil, S.A., Yao, M., Mai, C.J., Zou, Z., Scanlon, B.R., 1999. Results of Field Studies at the Maricopa Environmental Monitoring Site, Arizona. Rep. NUREG/CR-5694.US. Nuclear Regulatory Commission, Washington DC.

Zeleke, T.B., Si, B.C., 2006. Characterizing scale-dependent spatial relationships between soil properties using multifractal techniques. Geoderma 134, 440–452. http://dx.doi.org/10.1016/j.geoderma.2006.03.013.

Zimmermann, A., Schinn, D.S., Till, F., Elsenbeer, H., Zimmermann, B., 2013. Uncovering patterns of near-surface saturated hydraulic conductivity in an overland flow-controlled landscape. Geoderma 195, 1–11. http://dx.doi.org/10.1016/j.geoderma.2012.11.002.